RSC Advances

PAPER

Cite this: *RSC Adv.*, 2014, 4, 25993

Freeze-drying synthesis, characterization and *in vitro* bioactivity of chitosan/graphene oxide/hydroxyapatite nanocomposite

F. Mohandes[a] and M. Salavati-Niasari*[ab]

Polycrystalline and dispersed hydroxyapatite (HAP) nanoparticles were successfully prepared *via* a simple precipitation method with the aid of a new capping agent based on Schiff base compounds. After that, a composite of chitosan (CT), graphene oxide (GO) and HAP nanoparticles was synthesized by a freeze-drying method. The as-produced Schiff base, HAP nanoparticles, and CT/GO/HAP nanocomposite were analysed by several techniques including FTIR, SEM, HR-TEM, and XRD. In addition, the *in vitro* bioactivity of HAP nanoparticles and the CT/GO/HAP nanocomposite was evaluated by soaking them in simulated body fluid (SBF). By monitoring the changes of chemical composition of the SBF solutions, it was concluded that more Ca and P ions were released from the CT/GO/HAP nanocomposite compared to the pure HAP nanoparticles, indicating a high bioactivity of the nanocomposite. The SEM images showed that the formation and growth of apatite on the surfaces of the products increased after immersion for 14 days in SBF.

Received 18th April 2014
Accepted 30th May 2014

DOI: 10.1039/c4ra03534h

www.rsc.org/advances

Introduction

Hydroxyapatite ($Ca_{10}(PO_4)_6(OH)_2$, HAP), which belongs to the class of bioceramics, has been widely used in tissue engineering, orthopedics, drug and gene delivery systems, and protein separation due to its excellent biocompatibility and bioactivity with bone tissues, biodegradation and osteoconductivity.[1–3] Despite these advantages, the application of HAP for load bearing implants is restricted because of the peculiar brittleness and low fracture toughness of HAP.[4] Generally, there are two strategies to improve the mechanical properties of HAP. In the first way, HAP powders can be coated on a metallic implant surface,[5,6] and in the second way, HAP powders can be combined with different polymers. Several authors have addressed the use of biodegradable polymers including polylactic acid (PLA),[7] polyvinyl alcohol (PVA),[8] collagen,[9] polyethylene glycol (PEG)[10] and polymethylmethacrylate (PMMA)[11] was developed to prepare HAP nanocomposites.

So far, a great attention has focused on the composites of nano-sized HAP and chitosan (CT). CT is one of the most abundant polysaccharides consisting of β-(1-4)-2-deoxy-2-amino-D-glucopyranose units and β-(1-4)-2-deoxy-2-acetamino-D-glucopyranose units liked through 1-4 glycosidic bonds. CT is mainly produced by the partially deacetylation of chitin that can be extracted from crustacea. It is a suitable substrate for bioceramics due to its biocompatibility, biodegradability, and nontoxicity.[12–14] In addition, it has a high resistance upon heating due to the intramolecular hydrogen bonds formed between hydroxyl and amino groups.[15] Up to now, some improved tricomponent systems for tissue engineering scaffolds including alginate and collagen,[16] halloysite clay ($Al_2Si_2O_5(OH)_4 \cdot nH_2O$; $n = 0–2$),[17] and gelatin[18] with HAP/chitosan have been reported. As we know an ideal scaffold should not only have biocompatibility and mechanical properties matchable to those of natural bone, but also capabilities for response to specific biological signals expressing and promoting cell attachment, proliferation, differentiation and finally tissue regeneration.[19] Due to good electric conductivity, excellent biocompatibility, strong mechanical strength, light density and high stability, carbon materials in the form of nanotubes (CNTs), graphite and graphene (GR) sheets are promising reinforcing agents for polymeric matrix in bone tissue engineering.[20–22] In the structure of graphene nanosheets, a single layer of sp2-hybridized carbon atoms are packed together into a honeycomb two-dimensional (2D) lattice.[23] Compared to pristine graphene, graphene oxide (GO) is highly hydrophilic due to the presence of COOH and OH groups on the GO surface, yielding stable dispersion in water. Li *et al.* showed that the surface charges on GO are highly negative when dispersed in water by measuring the zeta potential due to the ionization of the carboxylic acid and the phenolic hydroxyl groups.[24] Therefore, the formation of stable GO colloids in water was attributed to not only its hydrophilicity but also the electrostatic repulsion.

---

[a] *Department of Inorganic Chemistry, Faculty of Chemistry, University of Kashan, P. O. Box. 87317-51167, Kashan, I. R. Iran. E-mail: salavati@kashanu.ac.ir; Fax: +98 361 5552935; Tel: +98 361 5912383*

[b] *Institute of Nano Science and Nano Technology, University of Kashan, Kashan, P. O. Box. 87317-51167, I. R. Iran*

Since graphene induces no obvious toxic effects *in vivo*,[25] functionalized GO with dopamine has been applied for hydroxyapatite mineralization.[26] On the other hand, the biocompatibility and applications of GO/HAP/PLA (polylactic acid) nanocomposites,[27] GO–Fe_3O_4 nanoparticle,[28] and GO–polyethylenimine[29] hybrid materials as drug and gene carriers were studied.

Freeze-drying has been shown to be a promising technique for preparing uniform fine-grained powders which can be sintered to very high densities.[30,31] This method has been successful in obtaining homogeneous, fine-grained and highly reactive Al_2O_3 and Fe_2O_3 powders.[31,32] In this work, subsequent freeze-drying was utilized to prepare HAp powders. The obtained HAp powders were then compacted and sintered to obtain the Hap ceramics.

By considering the hydrophilicity of GO, hydrophilic biopolymers including NH_2 and OH groups such as CT can be protonated to polycationic materials in acid media, which is favor of the interaction between polymer chains and GO sheets. Therefore, a good dispersion of GO in CT solution is expected.[33] It should be mentioned that the graphene/chitosan composites show a 200 times increase in the elasticity modulus compared to pure chitosan.[34] Keeping the as-mentioned points in view, present study was aimed to prepare a CT-functionalized GO/HAP nanocomposite scaffolds by freeze-drying method. A detailed structural and morphological characterization, as well as *in vitro* bioactivity of the nanocomposites were performed. The obtained results showed that the CT/GO/HAP nanocomposites have a much higher bioactivity rather than that of the pure HAP nanoparticles.

Experimental

Materials

All the chemicals with analytical grade were used as received. Salicylaldehyde, 2,2-dimethyl-propylendiamine, and methanol with analytical grade were used for the synthesis of Schiff base. Calcium nitrate tetrahydrate ($Ca(NO_3)_2\cdot 4H_2O$) and diammonium hydrogen phosphate ($(NH_4)_2HPO_4$) as calcium and phosphate sources were applied. In the synthesis method of HAP nanoparticles, NaOH was used for adjusting pH. Chitosan powder was purchased from Acros Organics (CT, degree of deacetylation = 82%, M_w = 100 000–300 000 g mol^{-1}). To prepare CT solution, acetic acid (100%, glacial) from Merck Company was used. To synthesize graphene oxide (GO), graphite powder, sulfuric acid (98%), nitric acid (67–70%), potassium permanganate ($KMnO_4$) and H_2O_2 (30%) were commercially available and employed without further purification. To prepare the SBF solution, NaCl, $NaHCO_3$, KCl, $K_2HPO_4\cdot 3H_2O$, $MgCl_2\cdot 6H_2O$, $CaCl_2$, Na_2SO_4, tris(hydroxymethyl)aminomethane ($(CH_2OH)_3CNH_2$) and HCl with analytical or reagent grades were purchased from Merck Company.

Synthesis of Schiff base

In this method, Schiff base was prepared by reaction between 2 mol of salicylaldehyde and 1 mol of 2,2-dimethyl-propylendiamine in 50 mL of methanol. The mixture was refluxed and heated at 70 °C for 3 h. After evaporating the solvent, crystallization was induced by adding petrol ether. Afterward, the crystals obtained were filtered on Buchner funnel. Pore diameter of the Whatman filter papers applied was 0.45 μm.

Synthesis of HAP nanoparticles

HAP nanoparticles were prepared by reaction between calcium–Schiff base solution and ammonium hydrogen phosphate solution. In the experiment, the molar ratios of Ca/Schiff base and Ca/P were 1.0 and 1.67, respectively. Details of the synthesis process are described. At first, 10 mmol of Schiff base was dissolved in 40 mL of methanol at 40 °C under a constant stirring of 1000 rpm. When Schiff base was completely dissolved in methanol, 10 mmol of $Ca(NO_3)_2\cdot 4H_2O$ was added into the solution. After that, additional stirring was performed for 30 min, and finally the yellow clear calcium–Schiff base solution was obtained. To prepare the ammonium hydrogen phosphate solution, 6 mmol of $(NH_4)_2HPO_4$ was dissolved in 40 mL of distilled water under magnetic stirring. A sodium hydroxide (NaOH) solution (0.1 M) was added dropwise into the ammonium hydrogen phosphate solution to adjust the pH of the solution to 12. At this time, the ammonium hydrogen phosphate solution was added slowly at a rate of 5 mL min^{-1} into the calcium–Schiff base solution. During the addition of the ammonium hydrogen phosphate solution into the calcium–Schiff base solution, a milky suspension was obtained. A round-bottom flask loaded with the resulting mixture was kept in an oil bath. The reaction mixture was heated at 120 °C for 5 h. After cooling the reaction mixture to room temperature, the final precipitates were collected by centrifugation at 4500 rpm for 5 min, washed three times with distilled water, methanol, and chloroform, sequentially. The white precipitates obtained were dried at 50 °C for 5 h. For comparison, the synthesis was carried out under the same preparation conditions without using any Schiff base. This experiment is named as blank test.

Synthesis of GO nanosheets

According to the previous work, GO was prepared by using graphite powder.[35] In this method, the improved Hummer method was applied to oxidize graphite for the synthesis of GO.[36] At first, 3 g of graphite powder, 18 mL of HNO_3, and 46 mL of H_2SO_4 were mixed and strongly stirred in the range of 0–5 °C for 15 min in a 500 mL reaction flask immersed in an ice-water bath. Then 6 g of $KMnO_4$ was added slowly into the above solution within 15 min. After this, the suspended solution was stirred continuously for 2 h in an ice-water bath and maintained the temperature in the range of 10–15 °C, and then the suspended solution was stirred continuously at 35 °C for half an hour. Subsequently, 138 mL of distilled water was a slowly added into the suspension within 10 min, and then the temperature was kept in the range of 95–98 °C for 30 min. Immediately, the suspension was diluted by 200 mL of warm distilled water (40 °C) and treated with 18 mL of H_2O_2 (30%) to reduce residual permanganate to soluble manganese ions.

Finally, the resulting suspension was filtered, washed with distilled water and dried in a vacuum oven at 60 °C for 24 h to obtain GO.

Synthesis of CT/GO/HAP nanocomposite

Since natural bone contains 70% HAP (inorganic phase) and ~30% collagen as connective protein, 70% of HAP, 29.9–30% of CT and 0.1% of GO was used as content of nanocomposite scaffold. CT/GO/HAP nanocomposites was synthesized by mixing three aqueous solutions. The preparation stages of the solutions are as follows: CT powder (1.50 g) was dissolved in 2% (v/v) aqueous acetic acid solution, and then the solution was stirred for 24 h to achieve a homogeneous suspension (solution I). This viscous solution was sonicated for 15 min to remove the air bubbles trapped in it. The as-synthesized GO powder (0.025 g) was dispersed in 50 mL DI water by sonication for 30 min (solution II). The as-synthesized HAP nanoparticles (3.0 g) was dispersed in 50 mL DI water by sonication for 30 min (solution III). By mixing the solutions I, II and III, a gray suspension was obtained, which was stirred for 24 h at room temperature (25 °C). The gray suspension was separated by centrifuging the suspension at 4500 rpm for 45 min, and dried in a freeze-dryer at −45 °C for 12 h.

Characterization

Fourier transform infrared (FTIR) spectra of the as-synthesized Schiff base, HAP nanoparticles and nanocomposites before soaking were obtained on a Magna-IR, spectrometer 550 Nicolet in KBr pellets in the range of 400–4000 cm^{-1}. In addition, the pellet forms soaked in the SBF solution were characterized by diffuse reflectance FTIR spectrometer (ATR-FTIR, Tensor 27, BRUKER) equipped with ATR system (reflection mode) in the range of 600–4000 cm^{-1}. Proton nuclear magnetic resonance (^{1}H-NMR) spectrum was obtained on a BRUKER (400 MHz) spectrometer. Proton chemical shifts are reported in ppm relative to an internal standard of Me_4Si. Powder X-ray diffraction (XRD) patterns were collected from a diffractometer of Philips Company with X'PertPro monochromatized Cu Kα radiation ($\lambda = 1.54$ Å, operated on 35 mA and 40 kV current). The diffraction angles (2θ) were scanned from 10° to 80°. SEM micrographs were taken by using a field-emission scanning electron microscope (HITACHI S4160, Japan). Energy dispersive spectrometry (EDS) analyses were studied by XL30, Philips microscope. Transmission electron images (TEM and HR-TEM) of HAP nanoparticles were recorded on a JEM-2100 with an accelerating voltage of 200 kV equipped with a high resolution CCD Camera. TEM images of CT/GO/HAP nanocomposite were obtained on a Philips EM208S transmission electron microscope with an accelerating voltage of 100 kV. In order to disperse GO powders in water, ultrasonic device was used. The dispersion was carried out at atmospheric pressure and ambient temperature with a multiwave ultrasonic generator (Sonicator 3000; Bandeline, MS 72, Germany), equipped with a converter/transducer and titanium oscillator (horn), 12.5 mm in diameter, operating at 20 kHz. Thermogravimetric analyses (TGA/DTG) were carried out with Pyris Diamond Perkin Elmer under air atmosphere at a heating rate of 10 °C min^{-1} from room temperature to 600 °C. Chemical analysis of the SBF solutions were determined by inductively coupled plasma-optical emission spectrometry (ICP-OES; Liberty 200, Varian, Clayton South, Australia).

In vitro bioactivity tests

Bioactivity of the as-produced HAP nanoparticles and CT/GO/HAP nanocomposites were evaluated *in vitro* by soaking in the SBF solution reported by Kokubo and Takadama.[37–39] The SBF solution was buffered at pH 7.40 by 50 mM tris(hydroxymethyl) aminomethane ($(CH_2OH)_3CNH_2$) and 45 mM HCl solution at 37 °C. In the bioactivity tests, 0.3 g of the powders were pressed into a pellet with thickness about 3 mm and diameter about 15 mm. The pellets washed, and dried were studied after soaking for 3, 7, 14, and 28 days. Besides, the concentrations of Ca, and P of the SBF solutions were analyzed by ICP spectroscopy.

Results and discussion

In this work, a new capping agent based on Schiff base compounds was synthesized and characterized by FTIR and ^{1}H-NMR spectroscopy. Fig. 1a shows chemical structure and starting reagents of the Schiff base used as capping agent. The FTIR and ^{1}H-NMR spectra of the Schiff base are seen in Fig. 1b and c, respectively. The FTIR spectrum exhibits a strong peak corresponding to the ν(C·N) at 1630 cm^{-1}, which proves the formation of Schiff base.[40] Details of ^{1}H-NMR spectrum of the Schiff base are as follows: ($CDCl_3$ as solvent): 1.084 ppm (s, 6H, 2 × CH_3), 3.498 ppm (s, 4H, 2 × CH_2), 6.895 ppm (t, 2H aromatic), 6.979 ppm (d, 2H aromatic), 7.271 ppm (d, 2H aromatic),

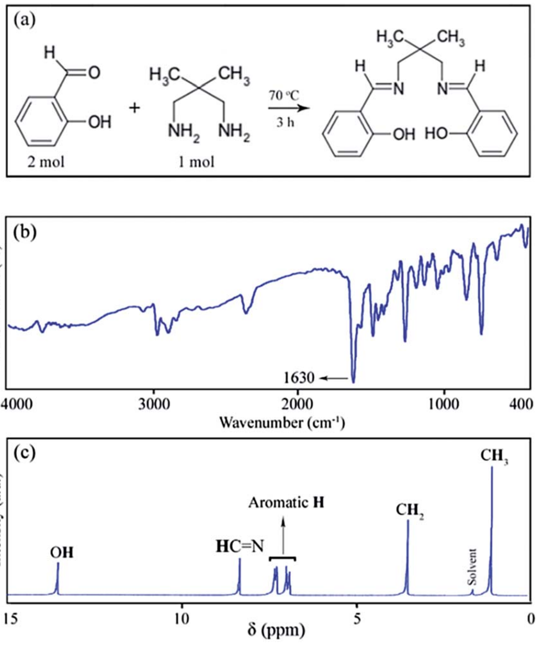

Fig. 1 (a) Chemical structure, (b) FTIR and (c) ^{1}H-NMR spectra of Schiff base.

7.328 ppm (t, 2H aromatic), 8.346 ppm (s, 2H, 2 × HC·N), 13.602 ppm (s, 2H, 2 × OH). No characteristic peaks of impurities like salicylaldehyde and 2,2-dimethyl-propylendiamine used as starting reagents are observed in the FTIR and ^{1}H-NMR spectra, indicating high purity of the as-synthesized Schiff base.

SEM image and EDS spectrum of HAP synthesized by Schiff base are seen in Fig. 2a and b, respectively. Morphology of HAP is composed of homogeneous nanoparticles. The EDS analysis clearly shows the presence of Ca, P and O elements in the product. The carbon signal comes from the EDS grid. Fig. 3a and b depict TEM and HR-TEM images of HAP nanoparticles. TEM observations show that the morphology of HAP crystals is nearly ellipsoid-like with particle sizes between 15-25 nm. The diffraction rings in the SAED pattern inserted in Fig. 3a indicates the polycrystalline nature of HAP nanoparticles. Moreover, the HR-TEM images show the clear (222) lattice fringes with the interplanar spacing of 0.194 nm. The typical TEM image of the product obtained from the blank test is seen in Fig. 3c. As shown in this figure, the poor crystalline particles are highly agglomerated, and it is difficult to measure the individual particle sizes. Therefore, it is found that the use of capping agent is a key factor to form dispersed and crystalline HAP nanoparticles.

Fig. 4 shows SEM images of GO nanosheets. The fully exfoliated GO sheets are different from graphitic platelets or pristine graphene sheets because of their low electrical conductivity due to presence of several oxygen containing groups on the surface of GO. Unlike graphene, GO sheets are expected to be "thicker" due to the presence of carbonyl, carboxyle, hydroxyle and epoxy groups above and below the original graphene planes.[35]

Fig. 5a–c display low and high magnification SEM images of CT/GO/HAP nanocomposite. The nanocomposite is highly porous with good interconnectivity, which is a favorable scaffold for cell attachment and new-bone formation.[40] The pore sizes of nanocomposite measured by SEM are between 20–50 μm. At higher magnification (Fig. 5c), the effective deposition and distribution of HAP nanoparticles onto CT-functionalized GO nanosheets can be clearly observed. The EDS spectrum of CT/GO/HAP nanocomposite in Fig. 5d shows the presence of Ca, P, O and C elements in the chemical composition of nanocomposite. To obtain further insight into the details of nanocomposite, TEM micrographs were taken and presented in Fig. 6. These images revealed appreciable aggregation of HAP nanoparticles on the surface of CT-functionalized GO nanosheets. The aggregation of HAP nanoparticles may be due to the electrically charged nature of chitosan network.

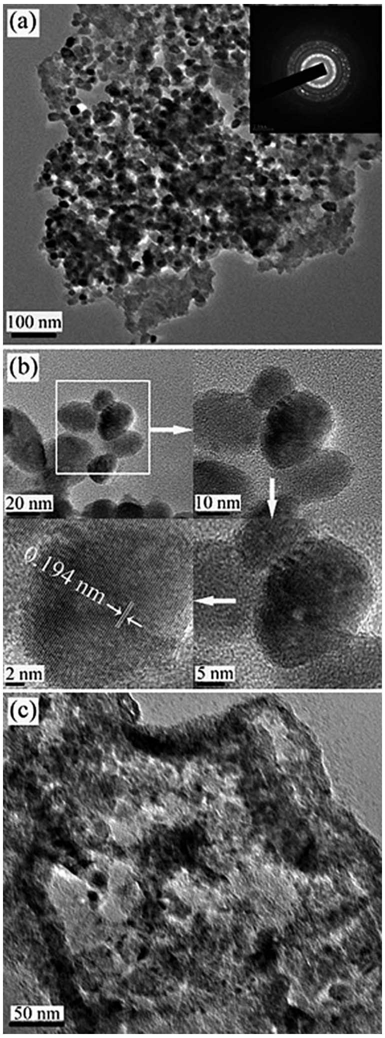

Fig. 3 (a) TEM and (b) HR-TEM images of HAP nanoparticles synthesized by Schiff base (SAED pattern is in the inset), (c) TEM image of HAP synthesized without using any Schiff base.

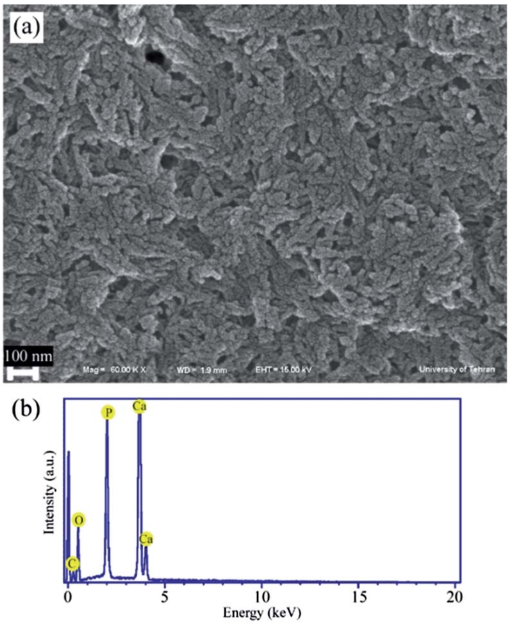

Fig. 2 (a) SEM image and (b) EDS pattern of HAP nanoparticles synthesized by Schiff base.

Thermal properties of GO nanosheets and CT/GO/HAP nanocomposite were investigated by TGA, and the TGA/DTG profiles are shown in Fig. 7. The weight loss of GO starts upon heating below 100 °C, which is attributed to the removal of water molecules adsorbed on the surface of GO (Fig. 7a). Moreover, there are two drops in weight around 150 and 250 °C.

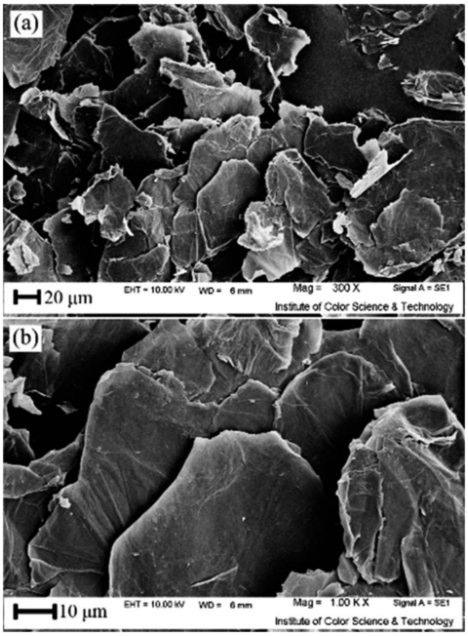

Fig. 4 (a and b) SEM images of GO nanosheets.

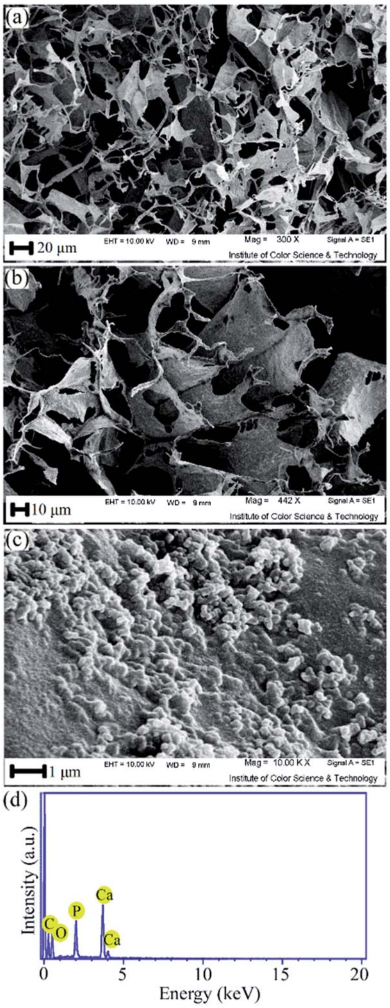

Fig. 5 (a–c) SEM images and (d) EDS pattern of CT/GO/HAP nanocomposite.

The former can be related to the evolution of CO and CO_2 from GO caused by the destruction of functional groups including oxygen atoms, and the latter is assigned to the combustion of the carbon skeleton of GO.[41] The TGA/DTG curves of CT/GO/HAP nanocomposite are seen in Fig. 7b. The initial drop in weight below 100 °C is attributed to the loss of adsorbed water. The significant weight loss around 310 °C can be due to the thermal decomposition of chitosan and combustion of GO.[41,42] It is noted that no notable occurrence of weight loss has been found for HAP nanoparticles, and they are very stable even at high temperature.[12]

The phase structure of the product was investigated by XRD. Fig. 8 displays the XRD patterns of GO nanosheets, pure CT, HAP nanoparticles and CT/GO/HAP nanocomposite before and after soaking in SBF. The reflection peaks in the XRD pattern of GO can be attributed to hexagonal phase carbon with space group of $P6_3/mmc$ and cell constants of $a = 2.4640$ Å, $b = 2.4640$ Å, and $c = 6.7360$ Å (JCPDS no. 08-0415). This pattern includes the characteristic reflection close to 12.5° and those observed at approximately 16.6°, 26.5° and 42.9°,[43] the strong and sharp peak at $2\theta = 11.7°$ corresponds to an interlayer distance of 7.6 Å (d001). The XRD pattern of pure CT shows the characteristic peak of chitosan with maximum intensity at $2\theta = 20.4°$.[44] All the diffraction peaks in the XRD pattern of HAP nanoparticles are well-matched to hexagonal phase hydroxyapatite with space group of $P63/m$ and cell constants $a = b = 9.4320$ Å, and $c = 6.8810$ Å, the apatite peaks were seen to occur at 2θ of 24.38, 31.64, 33.52, 36.12, 41.40, 54.81, 65.04 and 72.73, which are consistent with the standard XRD peaks for apatite (JCPDS-24-0033). By comparing the XRD patterns of CT/GO/HAP nanocomposite, pure CT, GO, and HAP, it can be seen that the characteristic peaks of HAP at 25.9° and 32.0° are available in the XRD pattern of nanocomposite. In addition, the characteristic peaks of CT and GO disappeared and a new peak at 29.6° appeared in the XRD pattern of nanocomposite, which may be attributed to the GO-grafted-CT network. When the –COOH groups of GO react with the $–NH_2$ groups of CT to form amide groups (–CONH–), the graft of GO and CT occurs. The XRD patterns of pure HAP and CT/GO/HAP nanocomposites after soaking for 14 days indicate the presence of hydroxyapatite. The low crystallinity of the new-formed hydroxyapatite crystals are responsible for the broadness of their diffraction peaks in the XRD pattern of HAP nanoparticles and CT/GO/HAP nanocomposite after soaking in SBF.

FTIR spectroscopy was employed to study the surface of GO, CT, HAP nanoparticles and CT/GO/HAP nanocomposite before and after soaking in SBF. The spectrum of GO (Fig. 9a) shows an intense peak at 3437 cm^{-1} due to the OH stretching vibration of absorbed water molecules and structural OH groups. Two adsorption peaks at 2922 and 2855 cm^{-1} are related to the asymmetric and symmetric stretching of C–H aliphatic. Also, this spectrum shows the presence of ν(C–O) at 1060 cm^{-1}, ν(C–O–C) at 1120 cm^{-1}, ν(C–OH) at 1380 cm^{-1}, ν(C·O) of carboxylic acid and carbonyl moieties at 1625 cm^{-1}. The adsorption peak at 1581 cm^{-1} may be attributed to the skeletal vibrations of

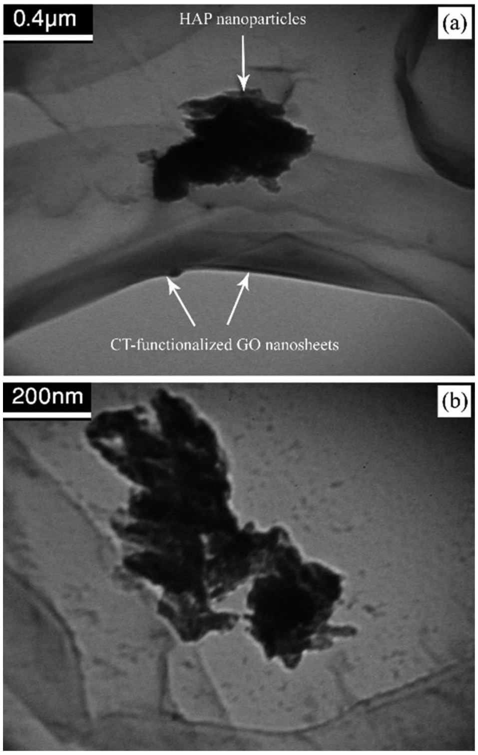

Fig. 6 (a and b) TEM images of CT/GO/HAP nanocomposite.

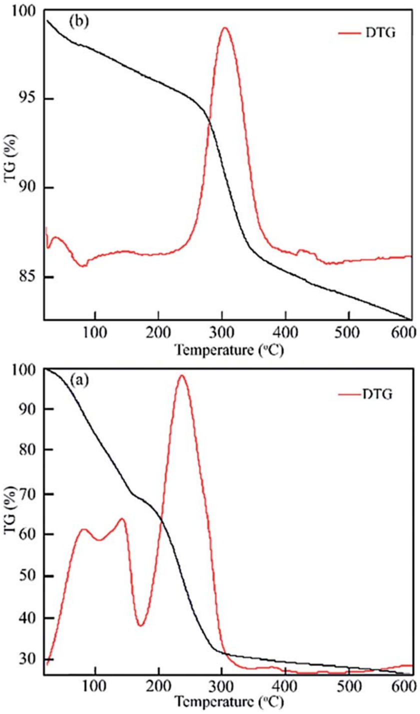

Fig. 7 TGA/DTG curves of (a) GO nanosheets and (b) CT/GO/HAP nanocomposite.

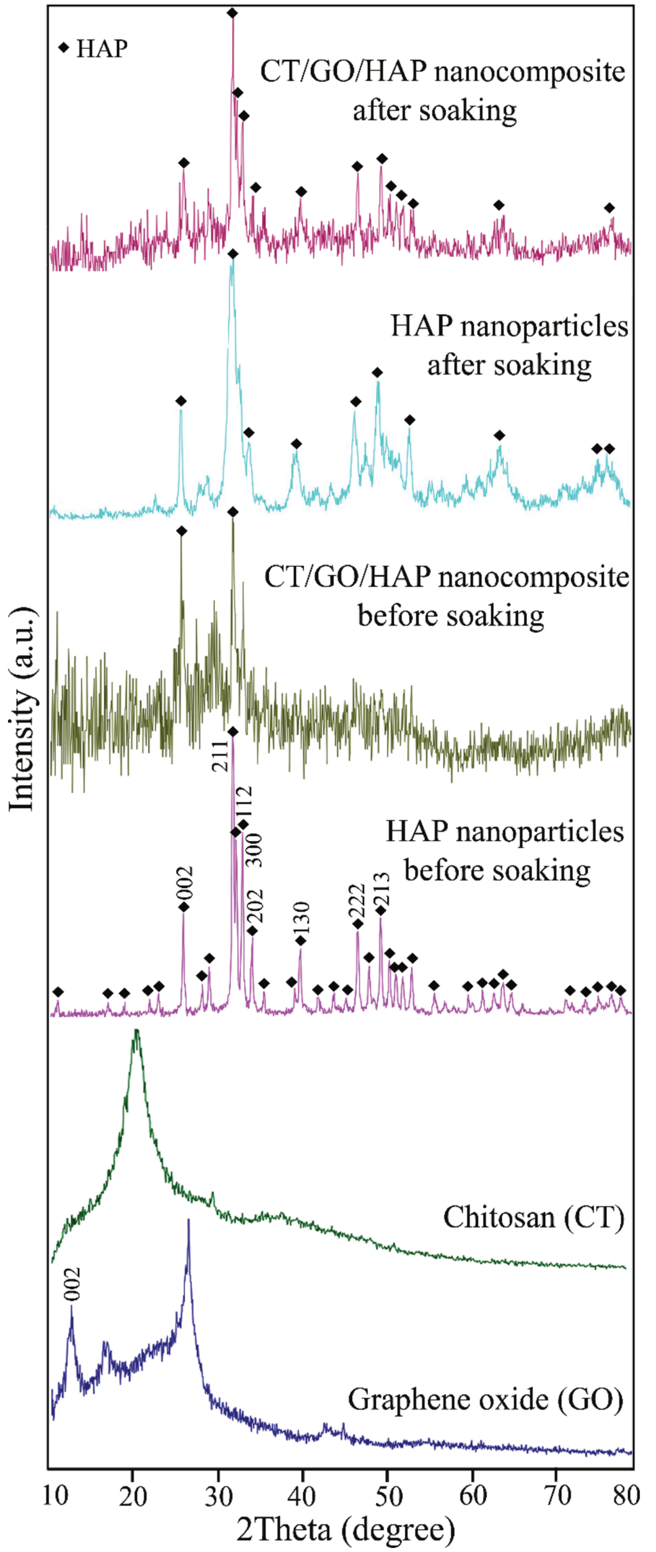

Fig. 8 XRD patterns of the products before and after soaking in SBF.

unoxidized graphitic domains.[35] In the FTIR spectrum of CT (Fig. 9b), the stretching vibrations of $\nu(NH_2)$ at 3427 and 1423 cm^{-1}, ν(C–H) at 2878 and 1380 cm^{-1}, ν(O–C–O) at 1083 and 1030 cm^{-1} are visible. The characteristic adsorption peaks of chitosan observed at 1637, 1593 and 1322 cm^{-1} are assigned to the amide I (C·O), amide II (–NH), and amino (NH_2).[40] Fig. 9c shows the FTIR of HAP nanoparticles. In this spectrum, the

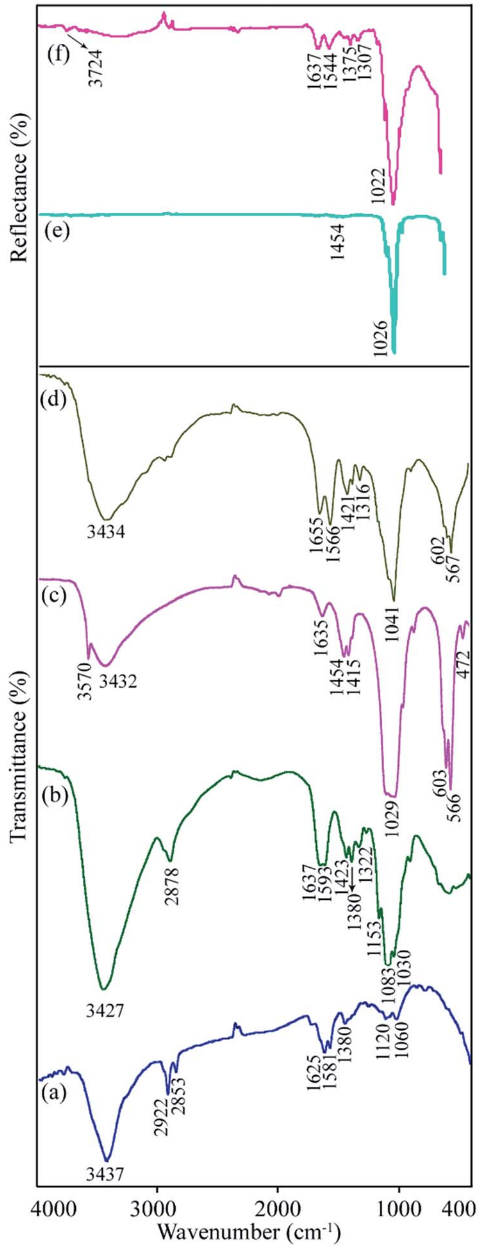

Fig. 9 FTIR spectra of (a) GO, (b) CT, (c) HAP nanoparticles, (d) CT/GO/HAP nanocomposite in the range of 4000–400 cm^{-1}. ATR-IR spectra of (e) HAP nanoparticles and (f) CT/GO/HAP nanocomposite after soaking in SBF in the range of 4000–600 cm^{-1}.

weak peak at 3570 cm^{-1} is due to the stretching vibration of OH groups in the structure of HAP. The adsorption bands attributed to the symmetric stretching (ν_2), asymmetric stretching (ν_3) and bending vibrations (ν_4) of the PO_4^{3-} ions are clear at 472, 1029, and around 566–603 cm^{-1}, respectively. The broad band at 3432 cm^{-1} (stretching vibration) and the weak band at 1635 cm^{-1} (bending vibration) are attributed to the crystal water and surface adsorbed water. The presence of the $\nu(\text{CO}_3^{2-})$ vibration at 1454 and 1415 cm^{-1} are observed in these spectrum, indicating the replacement of some PO_4^{3-} ions in HAP by CO_3^{2-} ions.[45] The carbonate ions might come from the atmosphere carbon dioxide which combined into the crystal structure during the dissolving and stirring processes. This evidence may improve the biological activity of the carbonated HAP, which is essential for bonding with natural bone.[46] FTIR spectrum of CT/GO/HAP before soaking in SBF includes the characteristic peaks of all the raw materials like GO, chitosan and HAP (Fig. 9d). By considering the FTIR of GO, CT and CT/GO/HAP nanocomposite, it can be seen that the adsorption peak attributed to the carboxylic acid (–COOH) in GO disappeared in the spectrum of CT/GO/HAP nanocomposite, and a new peak at 1655 cm^{-1} corresponding to amide group was detected, indicating the reaction of the –COOH groups of GO with the groups NH_2 of CT to form amide groups (–CONH–). On the other hand, the frequency of NH band shifted from 1593 (in pure CT) to 1566 cm^{-1} (in CT/GO/HAP nanocomposite) due to the formation of the amide groups. These phenomena prove the functionalization of GO by CT (CT-functionalized GO). On the basis of our experimental results, a scheme has been presented to describe the functionalization of GO by CT and formation of 3-D nanocomposite scaffold, as illustrated in Scheme 1. The formation of new HAP on the surface of the as-produced nanosized HAP and composite pellets after soaking in SBF for 14 days was studied by ATR-IR. In the spectrum of the HAP nanoparticles immersed in SBF (Fig. 9e), the strong peak of the $\nu_3(\text{PO}_4^{3-})$ at 1026 cm^{-1} and the $\nu(\text{CO}_3^{2-})$ at 1454 cm^{-1} are observed. The presence of the phosphate and carbonate vibrations indicates the formation of carbonated hydroxyapatite on the surface of the immersed pellets. The ATR-IR spectrum of CT/GO/HAP nanocomposite (Fig. 9f) the vibrations of OH, –CONH–, CO_3^{2-}, C–OH, C–O–C and PO_4^{3-} groups at 3724, 1637, 1544, 1375, 1307, and 1022 cm^{-1}, respectively. These results show the presence of carbonated HAP and CT-grafted-GO nanocomposite. By comparing the IR frequency of the amide

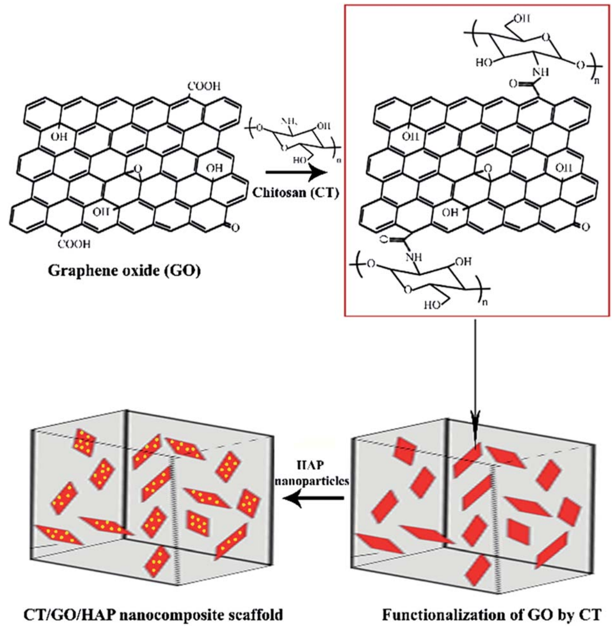

Scheme 1 Schematic representation of CT-functionalized GO/HAP scaffold as a 3-D nanocomposite.

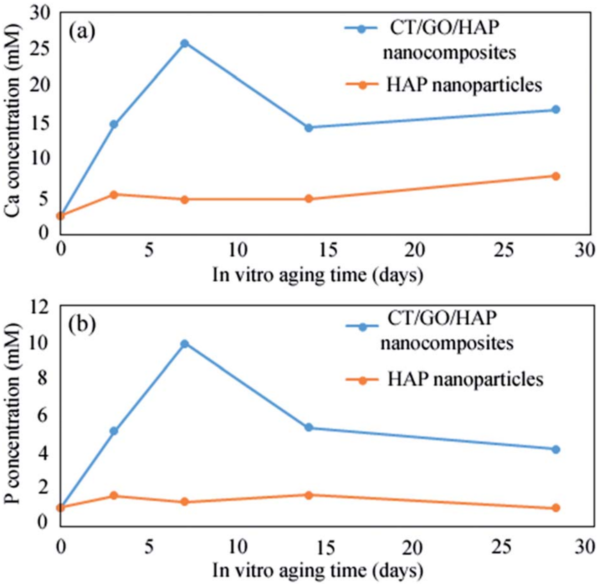

Fig. 10 (a) Ca and (b) P concentrations of SBF solutions *versus in vitro* aging time.

group before (1655 cm^{-1}) and after soaking in SBF (1637 cm^{-1}), it is concluded that this frequency decreased after soaking due to the interaction of the amide groups in CT/GO/HAP nanocomposite with the new-formed HAP nuclei.

Fig. 10a and b correlate the Ca and P concentrations of SBF solutions at different aging times, respectively. When the pellets of pure HAP nanoparticles and CT/GO/HAP nanocomposite are immersed in SBF, two main phenomena occur at the same time. They are the dissolution of the powders and precipitation of new apatite.[47] In case of CT/GO/HAP nanocomposite, from the beginning of immersion to 7 days, the dissolution process overcomes to the precipitation process due to the increase of the Ca and P concentrations in the SBF solutions. After 7 days of immersion, the Ca and P concentrations decrease due to the precipitation of apatite on the surface of the powders. After 14 days of immersion, the ion concentrations show a negligible changes. By considering the concentration changes of Ca and P, it can be seen that more Ca and P ions are releasing from the CT/GO/HAP nanocomposite compared to the pure HAP nanoparticles. Because thermodynamical stability of HAP nanoparticles is more than that of HAP nanocomposites, the dissolution rate of pure HAP nanoparticles is lower than that of HAP nanocomposites.[12] Besides, based on the XRD results, lower crystallinity of the CT/GO/HAP nanocomposite due to the presence of CT polymer leads to the increase of dissolution rate in composite.

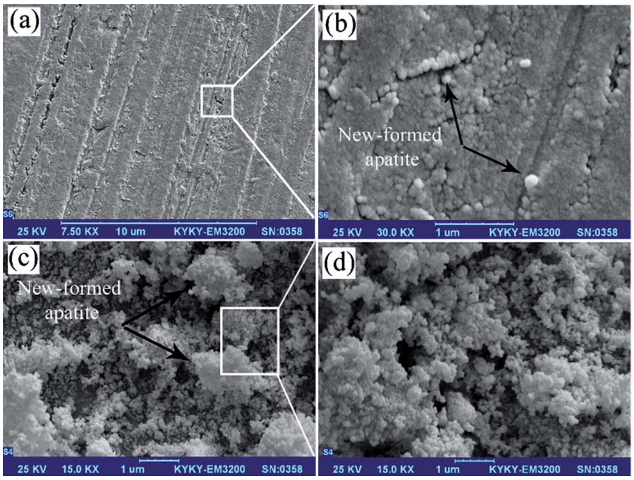

Fig. 11 Surface micrographs of (a and b) CT/GO/HAP nanocomposite and (c and d) HAP nanoparticles after immersing in SBF for 14 days.

New-formed apatite on the surface of the powder pressed into pellets was studied by visualizing change in morphologic features after immersing in SBF for 14 days using SEM. The SEM images of CT/GO/HAP nanocomposite (Fig. 11a and b) and HAP nanoparticles (Fig. 11c and d) show an increased growth of apatite after immersion for 14 days. This was due to the dissolution of HAP, and simultaneous precipitation of apatite. The grain sizes of the new-formed nanoparticles on the surface of the products are about 20–25 nm (Fig. 11b) and 10–15 nm (Fig. 11d).

Conclusions

Because of the hydrophilicity of GO, hydrophilic biopolymers including NH_2 and OH groups such as CT, the interaction between polymer chains and GO sheets is desirable and a good dispersion of GO in CT solution is expected, so, the graphene/chitosan composites show a 200 times increase in the elasticity modulus compared to pure chitosan.

In current work, at the first, Schiff base derived from salicylaldehyde and 2,2-dimethyl-propylendiamine was synthesized, and then applied as surfactant to fabricate HAP nanoparticles. After that, composite of chitosan, graphene oxide and hydroxyapatite nanoparticles were prepared by simple freeze-drying method and obtained results showed that the CT/GO/HAP nanocomposites have a much higher bioactivity rather than that of the pure HAP nanoparticles. The *in vitro* bioactivity of HAP nanoparticles and CT/GO/HAP nanocomposite was evaluated by soaking them in simulated body fluid (SBF). By monitoring the changes of chemical composition of the SBF solutions, it was concluded that more Ca and P ions released from the CT/GO/HAP nanocomposite compared to the pure HAP nanoparticles, indicating high bioactivity of the nanocomposite. The SEM images showed that the formation and growth of apatite on the surfaces of the products increased after immersion for 14 days in SBF.

Acknowledgements

Authors are grateful to council of University of Kashan for providing financial support to undertake this work.

Notes and references

1 L. L. Hench, *J. Am. Ceram. Soc.*, 1991, **74**, 1487.

2 M. Jarcho, *Clin. Orthop. Relat. Res.*, 1981, **157**, 259.

3 S. V. Joshi, M. P. Srivastava, A. Pal and S. Pal, *J. Mater. Sci.: Mater. Med.*, 1993, **4**, 251.

4 G. D. With, H. J. A. Van Dijk, N. Hattu and K. Prijs, *J. Mater. Sci.*, 1981, **16**, 1592.

5 J. H. Ni, Y. L. Shi, F. Y. Yan, J. Z. Chen and L. Wang, *Mater. Res. Bull.*, 2008, **43**, 45.

6 Z. Q. Yao, Y. Ivanisenko, T. Diemant, A. Caron, A. Chuvilin, J. Z. Jiang, *et al.*, *Acta Biomater.*, 2010, **6**, 2816.

7 T. Kasuga, Y. Ota, M. Nogami and Y. Abe, *Biomaterials*, 2000, **22**, 19.

8 G. Wu, B. Su, W. Zhang and C. Wang, *Mater. Chem. Phys.*, 2008, **107**, 364.

9 M. Kikuchi, T. Ikoma, S. Itoh, H. N. Matsumoto, Y. Koyama and K. Takakuda, *Compos. Sci. Technol.*, 2004, **64**, 819.

10 C. P. Dhanalakshmi, L. Vijayalakshmi and V. Narayanan, *Int. J. Phys. Sci.*, 2012, **7**, 2093.

11 H. Itokawa, T. Hiraide, M. Moriya, M. Fujimoto, G. Nagashima and R. Suzuki, *Biomaterials*, 2007, **28**, 4922.

12 R. Murugan and S. Ramakrishna, *Biomaterials*, 2004, **25**, 3829.

13 J. M. Oliveira, M. T. Rodrigues, S. S. Silva, P. B. Malafaya, M. E. Gomes and C. A. Viegas, *Biomaterials*, 2006, **27**, 6123.

14 J. Venkatesan and S. K. Kim, *Mar. Drugs*, 2010, **8**, 2252.

15 Y. L. Lee, E. Khor and C. E. Ling, *J. Biomed. Mater. Res., Part B*, 1999, **48**, 111.

16 C. C. Yu, J. J. Chang, Y. H. Lee, Y. C. Lin, M. H. Wu and M. C. Yang, *Mater. Lett.*, 2013, **93**, 133.

17 I. Deen, X. Pang and I. Zhitomirsky, *Colloids Surf., A*, 2012, **410**, 38.

18 Z. Babaei, M. Jahanshahi and S. M. Rabiee, *Mater. Sci. Eng., C*, 2013, **33**, 370.

19 K. Rodriguez, S. Renneckar and P. Gatenholm, *ACS Appl. Mater. Interfaces*, 2011, **3**, 681.

20 B. Zhao, H. Hu, S. K. Mandal and R. C. Haddon, *Chem. Mater.*, 2005, **17**, 3235.

21 A. A. White, S. M. Best and I. A. Kinloch, *Int. J. Appl. Ceram. Technol.*, 2007, **4**, 1.

22 T. K. Das and S. Prusty, *Journal of Research in Nanobiotechnology*, 2012, **1**, 019.

23 K. S. Novoselov, A. K. Geim, S. V. Morozov, D. Jiang, Y. Zhang, S. V. Dubonos, *et al.*, *Science*, 2004, **306**, 666.

24 D. Li, M. B. Muller, S. Gilje, R. B. Kaner and G. G. Wallace, *Nat. Nanotechnol.*, 2008, **3**, 101.

25 K. Yang, S. Zhang, G. Zhang, X. Sun, S. T. Lee and Z. Liu, *Nano Lett.*, 2010, **10**, 3318.

26 H. Liu, P. Xi, G. Xie, Y. Shi, F. Hou and L. Huang, *J. Phys. Chem. C*, 2012, **116**, 3334.

27 P. Marques, G. Gonçalves, M. K. Singh and J. Grácio, *J. Nanosci. Nanotechnol.*, 2012, **12**, 6686.

28 X. Y. Yang, Y. S. Wang and X. Huang, *J. Mater. Chem.*, 2011, **21**, 3448.

29 H. Kim, R. Namgung, K. Singha, I. K. Oh and W. J. Kim, *Bioconjugate Chem.*, 2011, **22**, 2558.

30 D. B. Hibbert and A. C. C. Tseung, *J. Mater. Sci.*, 1979, **14**, 2665.

31 L. A. Beyer, C. E. Kalnas, D. B. Roy and I. K. Lloyd, *Am. Ceram. Soc. Bull.*, 1987, **66**, 1647.

32 D. W. Johnson and F. J. Schnettler, *J. Am. Ceram. Soc.*, 1970, **53**, 440.

33 X. Yang, Y. Tu, L. Li, S. Shang and X. M. Tao, *ACS Appl. Mater. Interfaces*, 2010, **2**, 1707.

34 B. P. Lee, C. Y. Chao, F. N. Nunalee, E. Motan, K. R. Shull and P. B. Messersmith, *Macromolecules*, 2006, **39**, 1740.

35 F. Tavakoli and M. Salavati-Niasari, *J. Ind. Eng. Chem.*, DOI: 10.1016/j.jiec.2013.11.061.

36 W. S. Hummers and R. E. Offeman, *J. Am. Chem. Soc.*, 1958, **80**, 1339.

37 T. Kokubo and H. Takadama, *Biomaterials*, 2006, **27**, 2907.

38 I. Manjubala, S. Scheler, J. Bossert and K. D. Jandt, *Acta Biomater.*, 2006, **2**, 75.

39 G. Wei, J. T. Zhang and K. D. Jandt, *Carbon*, 2011, **49**, 2216.

40 W. W. Thein-Han and R. D. K. Misra, *Acta Biomater.*, 2009, **5**, 1182.

41 D. C. Marcano, D. V. Kosynkin, J. M. Berlin, A. Sinitskii, Z. Sun, A. Slesarev, *et al.*, *ACS Nano*, 2010, **4**, 4806.

42 G. Cardenas and S. P. Miranda, *J. Chil. Chem. Soc.*, 2004, **49**, 291.

43 S. Wakeland, R. Martinez, J. K. Grey and C. C. Luhrs, *Carbon*, 2010, **48**, 3463.

44 J. Venkatesan, Z. J. Qian, B. Ryu, N. A. Kumar and S. K. Kim, *Carbohydr. Polym.*, 2011, **83**, 569.

45 A. Kaflak, A. Slósarczyk and W. Kolodziejski, *J. Mol. Struct.*, 2011, **997**, 7.

46 P. Li, C. Ohtsuki and T. Kokubo, *J. Biomed. Mater. Res.*, 1994, **28**, 7.

47 M. Kheradmandfar, M. H. Fathi, M. Ahangarian and E. M. Zahrani, *Ceram. Int.*, 2012, **38**, 169.